doi:10.2109/jcersj2.15255

Effects of phase and doping on flash sintering of TiO_2

Yuanyao ZHANG, Jiuyuan NIE and Jian LUO

Department of NanoEngineering; Program of Materials Science and Engineering University of California, San Diego La Jolla, CA 92093, USA

Journal of the Ceramic Society of Japan 124 [4] 296-300 2016 Reprint

Journal of the Ceramic Society of Japan 124 [4] 296-300 2016 Full paper

Effects of phase and doping on flash sintering of TiO_2

Yuanyao ZHANG, Jiuyuan NIE and Jian LUO†

Department of NanoEngineering; Program of Materials Science and Engineering University of California, San Diego La Jolla, CA 92093, USA

Using TiO_2 as a model system, the effects of different doping (un-doped, V-doped vs. N-doped) and starting phases (anatase vs. rutile) on the flash sintering of TiO_2 are investigated. The doping and starting phase not only alter the onset flash sintering temperatures via changing the temperature-dependent electric conductivities of the green specimens, but also significantly affect the densification and microstructural development during the flash sintering. In all six cases, the coupled thermal and electric runaway temperatures predicted from measured specimen conductivities agree well with the observed onset flash temperatures (with less than 5°C in differences), supporting a recently-developed quantitative model.

Key-words : Flash sintering, Titanium dioxide, Thermal runaway

[Received October 29, 2015; Accepted February 11, 2016]

1. Introduction

Raj and co-workers invented "flash sintering" as a novel sintering technology that enables rapid densification at low furnace temperatures.[1),2)] Recent studies showed that flash sintering could be applied to a variety of materials, including nominally-pure oxides of ZnO,[3)–5)] ZrO_2,[6)] TiO_2,[7)] and Y_2O_3,[8)] as well as Y_2O_3-doped ZrO_2,[9)] Bi_2O_3-doped ZnO,[4)] MgO-doped Al_2O_3,[10)] MnO_2-doped SnO_2,[11)] Gd_2O_3-doped CeO_2,[12)] and SiC–Al_2O_3–Y_2O_3 composites.[13)] In a typical flash sintering experiment, an (initially-constant) electric field is applied to a specimen that is placed in a furnace; then, the furnace temperature is increased at a constant ramp rate, until the occurrence of a "flash" event with a sudden increase of the electric current, leading to an abrupt rise in the specimen temperature; after a few seconds, the power control switches from a constant-voltage to a constant-current mode with a pre-set maximum current that limits the steady-state temperature during the sintering; the specimen is typically kept for a few seconds at this steady state before the sintering is completed.

Recently, we proposed that the onset flash occurs as a coupled thermal and electric runaway.[3),4)] We further developed a quantitative model that can accurately predict the onset flash temperatures, where we used ZnO in several different oxidizing and reducing atmospheres as the model systems to test and validate this proposed model.[3),4)] Similar thermal runaway models have been proposed by Todd et al.[14)] and by Dong and Chen,[15),16)] which are based on the same physical concepts but used somewhat different mathematical approaches to solve the thermal runaway conditions (noting that the reports[14),15)] from both groups were submitted after the initial submission, but before the publication, of our first report of this quantitative thermal runaway model;[4)] thus, all three models[4),14),15)] have been developed independently).

Jha and Raj first reported the flash sintering of nominally-pure rutile TiO_2.[7)] In this study, we further investigated the flash sintering of both rutile and anatase TiO_2 specimens, including nominally-pure (undoped) specimens as well as representative cation (V) and anion (N) doped specimens with approximately identical starting particle sizes and green densities. Specifically, we showed that six TiO_2 specimens have different temperature-dependent conductivities, leading to different onset flash sintering temperatures. We have further demonstrated that the coupled thermal and electric runaway temperatures predicted from our prior quantitative model[4)] agree with the observed onset flash temperatures within 5°C for all six cases, which critically supports our prior model.[4)] Finally, we also demonstrated that the initial phase and doping can critically affect the microstructural development during the flash sintering.

2. Experimental

Anatase (99.98% purity, ~30 nm particle size) and rutile (99.9% purity, ~30 nm particle size) powders were purchased from US Research Nanomaterials. Inc. (Houston, TX, USA). To prepare V-doped powders, we adopted a well-established procedure to make TiO_2-supported V_2O_5 monolayer catalysts.[17),18)] Specifically, the pure anatase or rutile powder was mixed with an aqueous solution of NH_4VO_3 and NH_4OH and dried in oven at 85°C for 12 h. Then, the mixed powders were annealed at 220°C for 3 h (to remove moisture), at 450°C for 3 h in an open container, and at 500°C for 4 h in a closed container; the annealed powders were subsequently air quenched.

N-doped TiO_2 powders were prepared by annealing TiO_2 powders in flowing ammonia following a surface nitridation procedure in Ref. 19). Specifically, the pure anatase or rutile powder was placed in a tube furnace and purged with argon for 1 h. The powders were annealed at 250°C for 1 h to remove moisture, before the furnace temperature was raised to 450°C and the flowing gas was switched to ammonia. Subsequently, the specimens were annealed in flowing ammonia isothermally for 7 h and cooled in furnace with flowing argon.

Six different powders, including un-doped, N-doped, and V-doped anatase and rutile, were used to prepare specimens for flash sintering experiments. All powders were uniaxially pressed at ~200 MPa to make green specimens with the approximate dimensions: D (diameter) = 6.4 mm and H (height) = 1 mm. The average bulk densities of the green specimens were measured to be ~45% of the theoretical density. The relatively low green

† Corresponding author: J. Luo; E-mail: jluo@alum.mit.edu

‡ Preface for this article: DOI http://dx.doi.org/10.2109/jcersj2.124.P4-1

DOI http://dx.doi.org/10.2109/jcersj2.15255

densities were due to two reasons, as follows. First, the green specimens were pressed at a relatively low pressure of 200 MPa to make sure the specimen surfaces were flat and specimens are homogenous. Second, we used nanosized powders, which also contributed to the low green densities. However, we emphasize that the low green densities should not influence the comparison of the flash sintering results because all six specimens had roughly identical green densities. Pt electrodes were sputtered on both sides of green specimens using a Denton Discovery 18 sputtering system and the surrounding areas were slightly grounded. The specimens were placed in a horizontal tube furnace and attached with Pt wires on both sides. In the flash sintering experiments, an initially-constant electric field of 500 V/cm was applied, and the specimens were heated with a constant ramp rate of 5°C per minute. In each individual experiment, a flash event occurred, after which the electric power source switched from the constant-voltage control mode to the constant-current control mode with a preset maximum value of $I_{max} = 0.5$ A (corresponding to an estimated current density of $J_{max} \approx 20\,mA/mm^2$). Subsequently, the furnace and the power supply were shut down ~30 s after the current reached the maximum value, and the specimens were cooled in the furnace. Final bulk densities were measured by the standard Archimedes method. The microstructures were characterized by a FEI ultra-high resolution scanning electron microscope (SEM, Hillsboro, OR, USA). The specimens were characterized by X-ray diffraction (XRD) using a Rigaku (Tokyo, Japan) RU 200-BH diffractometer.

As we will show later, all anatase specimens were converted to the rutile phase after the flash sintering, but they are often referred to as un-doped, V-doped and N-doped anatase specimens (based on the starting phase) to differentiate them from those specimens prepared by the rutile powders.

3. Results and discussion

3.1 Specimen conductivities and their effects on onset flash sintering

Figure 1(a) displays the electric power density vs. the furnace temperature (T_F) curves for the six specimens (i.e., un-doped, N-doped, and V-doped anatase and rutile) during the flash sintering experiments. Figure 1(b) shows the Arrhenius plots of measured conductivities of the same six specimens, where specimen temperatures were estimated from the black-body radiation model following the work of Raj.[20] There is a clear correlation between the measured specimen conductivities [Fig. 1(a)] and flash sintering behaviors [Fig. 1(b)]; higher conductivities lead to the occurrence of flash sintering at lower temperatures.

As shown in Fig. 1 and summarized in **Table 1**, the onset flash sintering temperature of undoped anatase (768°C) was appreciably lower than that of undoped rutile (831°C). The cation doping of vanadium (V) consistently reduced the onset flash sintering temperatures of both rutile and anatase specimens [Fig. 1(a)] by substantially increasing the conductivities [Fig. 1(b)]. Specifically, V doping reduced the onset flash sintering temperature of the anatase specimen by >100°C from 768 to 665°C, and it reduced the onset flash sintering temperature of the rutile specimen by >150°C from 831 to 672°C. Interestingly, the effects of anionic doping of nitrogen (N) were different for anatase and rutile specimens; N doping increased the onset flash sintering temperature of the anatase specimen by ~50°C, from 768 to 818°C, but decreased the onset flash sintering temperature of the rutile specimen by ~57°C, from 831 to 774°C.

The effects of phase and doping on changing conductivities and subsequently onset flash sintering temperatures are worthy some further discussion. According to our model (that will be discussed in detail below), the onset flash sintering temperature depends solely on the temperature-dependent conductivities of the actual specimens, which in turn depend on both the intrinsic

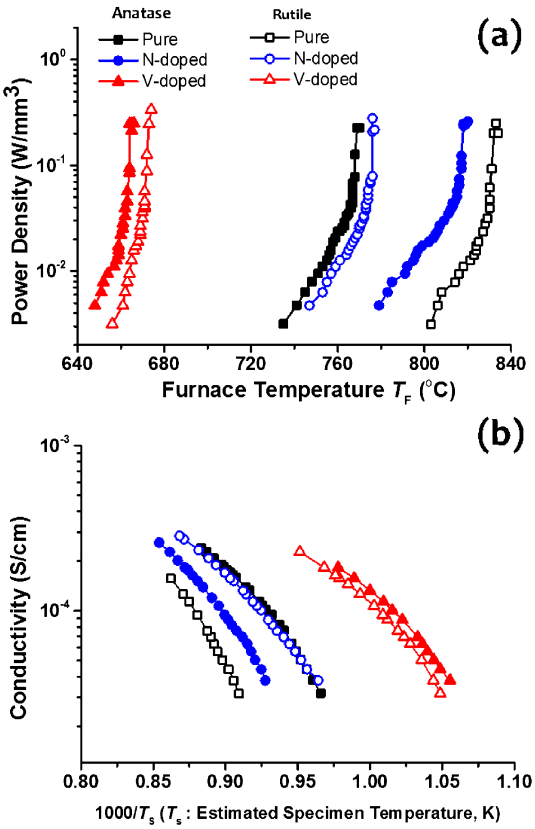

Fig. 1. (a) Measured electric power dissipation vs. furnace temperature curves for the flash sintering of six different TiO_2 specimens, where the initial applied electric field was set to be 500 V/cm and current limit was set to be 0.5 A. (b) Measured conductivity vs. the reciprocal of the estimated specimen temperature curves.

Table 1. Summary of key results of the flash sintering experiments

Starting Phase	Doping	Observed Onset Flash Temperature ($T_{F,0}^{(exp)}$, °C)	Predicted Thermal Runway Temperature ($T_{F,0}^{(predicted)}$, °C)	Estimated Steady-State Specimen Temperature ($T_S^{(ss)}$, °C)	Final Relative Density (%)	Final Grain Size (mean ± STD, μm)
Anatase	undoped	768	766	1039	95	1.11 ± 0.12
	V-doped	665	661	992	86	1.10 ± 0.27
	N-doped	818	815	1077	92	0.38 ± 0.05
Rutile	undoped	831	827	1064	97	0.46 ± 0.08
	V-doped	672	670	1078	96	1.04 ± 0.29
	N-doped	774	773	1061	87	0.21 ± 0.05

bulk conductivities as well as the surface and grain boundary conductivities, particle sizes, and porosity. Anatase has higher conductivities than rutile so that the flash sintering of anatase specimens started at lower temperatures. Cation doping with V (that is typically an electron donor for TiO_2) will increase the conductivities of both anatase and rutile substantially, promoting the flash sintering in both materials. N doping has opposite effects on anatase and rutile; it increases the rutile conductivities (promoting the flash sintering) but decreases the anatase conductivities (deferring the flash sintering). This may be explained by different surface vs. bulk doping effects; further investigations are warranted to clarify the exact mechanisms.

3.2 The coupled thermal and electric runaway model for predicting the onset flash sintering temperatures

Although the effects of starting phase and doping on the conductivities of TiO_2 specimens are rather complex, this study demonstrated that the measured conductivities can be used to predict the coupled thermal and electric runaway temperatures using a recently-developed quantitative model[3),4)] that agree well with the observed onset flash sintering temperatures in all six cases, as follows. In this model,[3),4)] the rise of specimen temperature is determined by the energy conservation law. The specific conditions for stable and unstable temperature rises are elaborated as follows. The necessary and sufficient conditions for a stable temperature rise are:

$$\sigma(T_S)E^2V_S = \dot{Q}(T_S, T_F) \tag{1}$$

and

$$E^2V_S\left.\frac{d\sigma}{dT}\right|_{T_S} < \frac{\partial\dot{Q}(T_S, T_F)}{\partial T_S}, \tag{2}$$

where E is the electrical field, V_S is the volume of the specimen, T_S and T_F are the specimen (S) and furnace (F) temperatures, respectively, and $\sigma(T_S)$ is the specimen conductivity. In Eq. (1), the left side, $\sigma(T_S)E^2V_S$, is the rate of heat generation from joule heating, whereas the right side, $\dot{Q}(T_S, T_F)$, represents the rate of heat dissipation from the specimen. Eq. (2) represents the condition for a stable temperature rise, whereas an unstable temperature rise will occur if

$$E^2V_S\left.\frac{d\sigma}{dT}\right|_{T_S} > \frac{\partial\dot{Q}(T_S, T_F)}{\partial T_S}. \tag{3}$$

Thus, the full conditions for the occurrence of a coupled thermal and electric runaway are:

$$\begin{cases} \sigma(T_S)E^2V_S = \dot{Q}(T_S, T_F) \\ E^2V_S\left.\frac{d\sigma}{dT}\right|_{T_S} = \frac{\partial\dot{Q}(T_S, T_F)}{\partial T_S} \equiv \alpha \\ E^2V_S\left.\frac{d^2\sigma}{dT^2}\right|_{T_S} > \frac{\partial\alpha}{\partial T_S} = \frac{\partial^2\dot{Q}(T_S, T_F)}{\partial T_S^2} \end{cases}, \tag{4}$$

The above thermal runaway conditions were proposed in our prior model[3),4)] but written more explicitly here. The first equation in Eq. (4), which is identical to Eq. (1), is the energy conservation law. The second equation in Eq. (4) is the stability condition that defines the transition from a stable temperature rise [Eq. (2)] to an unstable [Eq. (3)] temperature rise. The third condition in Eq. (4), which was given for the first time in this paper, is to ensure that Eq. (4) are sufficient conditions for a coupled thermal and electric runaway to occur [because this third condition, along with the first two equations in Eq. (4), guarantees that Eq. (2) is satisfied at lower temperatures while Eq. (3) is satisfied at higher temperatures, but not vice versa].

The rate of heat dissipation from specimen, $\dot{Q}(T_S, T_F)$, can be quantified for heat conduction, convention, and radiation, if the geometry and all heat transfer parameters are known. For a case where black body radiation is the dominant heat dissipation mechanism, a simple analytic form can be obtained:

$$\frac{\partial\dot{Q}(T_S, T_F)}{\partial T_S} \equiv \alpha = 4\varepsilon\sigma_{\text{Stefan}}T_S^3A_s \tag{5}$$

where A_S is the surface area of the specimen, $\sigma_{\text{Stefan}} = 5.67 \times 10^{-8}\,\text{W/m}^2\text{K}^4$, and ε is the emissivity (assuming $\varepsilon \approx 1$ for simplification in this study). In this simplified case (that is used as an approximation), Eq. (5) is only a function of specimen temperature (T_S); thus, the coupled thermal and electric runaway condition can be determined by the following two conditions:

$$\begin{cases} E^2V_S\left.\frac{d\sigma}{dT}\right|_{T_S} = \alpha \approx 4\sigma_{\text{Stefan}}T_S^3A_s \\ E^2V_S\left.\frac{d^2\sigma}{dT^2}\right|_{T_S} > \frac{d\alpha}{dT_S} \end{cases}, \tag{6}$$

The above equations can be solved graphically by plotting $E^2V_S(d\sigma/dT)_{T_S}$ and $4\sigma_{\text{Stefan}}T_S^3A_s$vs. T_S curves and finding their intersections to obtain the specimen temperature (T_S) at the onset flash/thermal runaway, as shown in **Fig. 2** for the six cases of TiO_2 based systems in this study as well as for ZnO based systems in two prior studies.[3),4)] Subsequently, the corresponding furnace temperature (T_F) can be solved from T_S using Eq. (1). It is worth noting that the thermal runaway models proposed slightly later by Todd et al.[14)] and by Dong and Chen[15),16)] were essentially based on the same physical concepts as this (our prior) model,[3),4)] although the specific mathematical approaches (the specific equations and methods used) to solve the onset flash sintering (thermal runaway) temperatures are somewhat different.

Figure 2 shows the computed differential heat generation rates $[E^2V_S(d\sigma/dT)_{T_S}]$ vs. specimen temperature (T_S) curves for the six TiO_2 specimens, which were calculated based on the Arrhenius fitting of the conductivities shown in Fig. 1(b). In Fig. 2, we also plot the computed differential heat dissipation rate ($4\sigma_{\text{Stefan}}T_S^3A_s$) vs. specimen temperature curve (the grey solid line). The intersections of the solid and dotted/dashed lines represent the specimen temperatures (T_S) at the occurrences of coupled thermal and electric runaways; subsequently, the corresponding furnace temperatures ($T_{F,0}^{(\text{predicted})}$) were estimated from black body radiation model, assuming ideal black body radiation. These predicted furnace temperatures ($T_{F,0}^{(\text{predicted})}$) are consistent with observed onset flash temperatures ($T_{F,0}^{(\text{exp})}$) within 5°C for all six cases (Fig. 2 and Table 1).

The excellent agreements to somewhat surprisingly-high precisions (<5°C in these six cases) are due to several factors discussed in the prior report,[4)] e.g., the errors of temperature measurements by the thermocouple were largely canceled since we used the conductivities that were measured in situ for the prediction. The exponential dependence of conductivities on temperature also made the prediction less sensitive to other errors. The predicted $T_{F,0}^{(\text{predicted})}$ values are lower than the observed onset flash temperatures for all six cases, which are likely due to the non-linearity in Fig. 1(b) (that is presumably due to the partial sintering of TiO_2 specimens before the onset of flash); thus, the extrapolations underestimated the specimen conductivities slightly in general because of the concave curvatures in Fig. 1(b). Nonetheless, the excellent agreements between predicted $T_{F,0}^{(\text{predicted})}$ and observed $T_{F,0}^{(\text{exp})}$ for all six cases provided a further strong support for the recently-developed quantitative

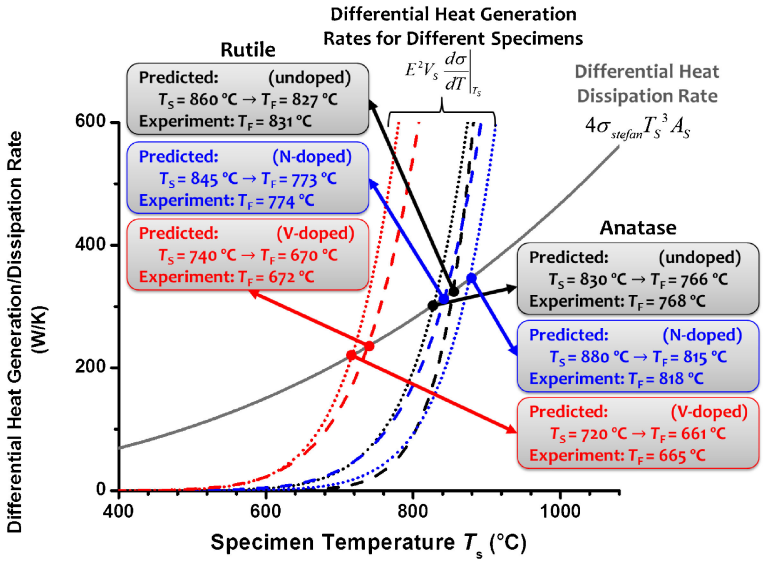

Fig. 2. Computed differential heat generation rates vs. specimen temperature curves for the six TiO_2 specimens, along with the computed differential heat dissipation rate vs. specimen temperature curve (represented by the solid grey line). The anatase specimens are represented by dotted dashed lines, whereas the rutile specimens are represented by dashed lines. The intersections of the two types of curves represent the predicted coupled thermal and electric runaway conditions; see text, as well as the original article[4] that proposed this model, for elaboration.

model for predicting onset flash temperatures,[3),4)] and attested that the flashes also start as coupled thermal and electric runaway for these six TiO_2 based specimens with different starting phase and doping.

3.3 Densification

The relative densities after flash sintering and estimated specimen temperatures in the steady states (during the ~30 s' sintering after the current reached the maximum value) are listed in Table 1. The densities of undoped anatase and rutile specimens after ~30 s of flash sintering were 95 and 97%, respectively, of the theoretical density of the rutile phase. The final density of the specimen that was made of the undoped anatase powder was slightly lower than that made of the undoped rutile powder initially, which may be related to the anatase-to-rutile phase transformation that is associated with a volumetric shrinkage. The anionic doping of N reduced the final densities to 92% (for the anatase specimen) and 87% (for the rutile specimen), respectively, while the estimated temperatures in steady states are comparable (Table 1). The cationic doping of V reduced the onset flash sintering temperatures of the anatase and rutile specimens substantially; the estimated temperature in the steady state is 992°C for the V-doped anatase specimen (being lower than that for the undoped anatase specimen), which resulted in a lower relative density of 86%; in contrast, the estimated temperature in the steady state for the V-doped rutile specimen is 1078°C, which is similar to that for the undoped rutile specimen; thus, the flash-sintered V-doped rutile specimen also has a high relative density of ~96%.

3.4 Phase transformation during flash sintering for anatase specimens

XRD patterns in **Fig. 3** show that all three anatase specimens transferred to the rutile phase after the flash sintering. For brevity, these specimens are still called as un-doped, V-doped, and N-doped anatase specimens (according to the phase in initial powders before flash sintering), to differentiate them from the specimens prepared by un-doped, V-doped, and N-doped rutile powders.

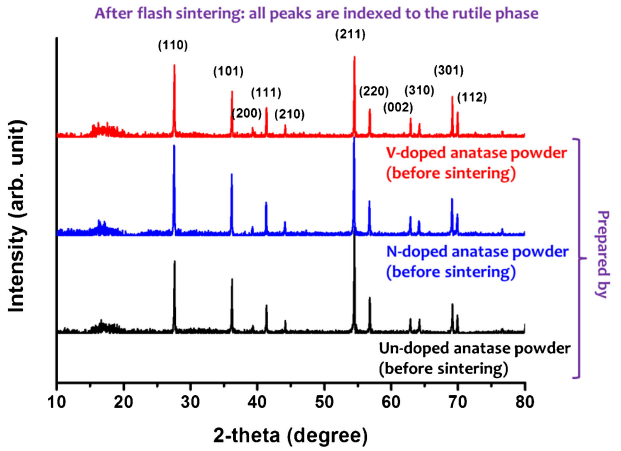

Fig. 3. XRD patterns of three flash-sintered specimens prepared with un-doped, V-doped and N-doped anatase powders, showing that all specimens were converted to the rutile phase after the flash sintering. For brevity, these specimens are still referred to as un-doped, V-doped and N-doped anatase specimens in text (to differentiate them from the specimens prepared by un-doped, V-doped and N-doped rutile powders).

3.5 Microstructures

Figure 4 shows the microstructures of the fractured surfaces of the six flash-sintered specimens. Although the undoped anatase and rutile specimens (noting they both contain the rutile phase after flash sintering) have similar estimated temperatures in their steady states, their microstructures are different. The flash-sintered undoped anatase specimen have (clustered) secondary particles of 1.11 (mean) ± 0.12 (one standard deviation) μm, which are composed of smaller primary grains, the boundaries of which are not clearly distinguishable in the SEM image [Fig. 4(a)] so that we cannot measure the exact grain size; this

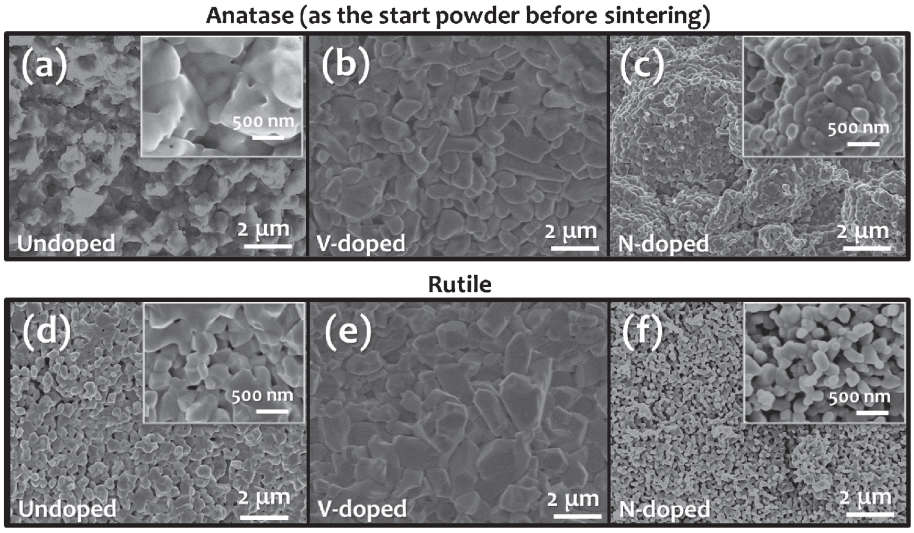

Fig. 4. SEM images of representative microstructures of the fractured surfaces of the flash-sintered specimens that were prepared using (a) un-doped, (b) V-doped, and (c) N-doped anatase powders, as well as (d) un-doped, (e) V-doped, and (f) N-doped rutile powders. All specimens are rutile after the flash sintering.

meatball-like microstructure (with hierarchical primary and secondary particles/grains at two different length scales) is presumably due the anatase-to rutile phase transformation that created extra porosity.[21] In contrast, the undoped rutile specimen has a (relatively uniform) grain size of $0.46 \pm 0.08\,\mu m$ after the flash sintering. We note that we did not observe any significant difference in the agglomeration in the starting powders; thus, we attribute clustered (meatball-like) structures in Fig. 4 to the anatase-to-rutile phase transformation that created extra porosity. A similar sintered microstructure was observed for Al_2O_3 and attributed to a similar phase transformation mechanism in a prior study.[21]

The grain sizes of the V-doped anatase and rutile specimens, respectively, are 1.10 ± 0.27 and $1.04 \pm 0.29\,\mu m$, respectively. The grain size of N-doped anatase is $0.38 \pm 0.05\,\mu m$, with a meatball-like microstructure. The N-doped rutile specimen has a substantially smaller grain size of $0.21 \pm 0.05\,\mu m$ after the flash sintering, which is related to the low relative density of ~87%.

4. Conclusions

In summary, we investigated the flash sintering of six TiO_2 based specimens with different doping (un-doped, V-doped vs. N-doped) and initial phases (anatase vs. rutile). In all six cases, the coupled thermal and electric runaway temperatures predicted from the measured specimen conductivities agree well with the observed onset flash temperatures within 5°C, supporting a recently-developed quantitative model.[4] The doping and initial phase also appreciably affect the densification and microstructural development during the flash sintering.

Acknowledgement The work of flash sintering and controlling high-temperature grain boundaries and microstructural development with electric fields is supported by the Aerospace Materials for Extreme Environments program of the U.S. Air Force Office of Scientific Research (AFOSR) under the grant no. FA9550-14-1-0174 and we thank our AFOSR program manager, Dr. Ali Sayir, for his support and guidance. J.N. also thanks partial support from the NSF under the grant no. CMMI-1436305 for his research on conventional sintering and processing of TiO_2 (including the effects of the anatase-to-rutile phase transformation), which helped to understand the development of unique meatball-like microstructures [Figs. 4(a) and 4(c)] with similar underlying mechanisms between the flash and conventional sintering.

References

1) M. Cologna, B. Rashkova and R. Raj, *J. Am. Ceram. Soc.*, **93**, 3556–3559 (2010).
2) R. Raj, M. Cologna and J. S. C. Francis, *J. Am. Ceram. Soc.*, **94**, 1941–1965 (2011).
3) Y. Zhang and J. Luo, *Scr. Mater.*, **106**, 26–29 (2015).
4) Y. Zhang, J.-I. Jung and J. Luo, *Acta Mater.*, **94**, 87–100 (2015).
5) C. Schmerbauch, J. Gonzalez-Julian, R. Roeder, C. Ronning and O. Guillon, *J. Am. Ceram. Soc.*, **97**, 1728–1735 (2014).
6) J. S. C. Francis and R. Raj, *J. Am. Ceram. Soc.*, **95**, 138–146 (2012).
7) S. K. Jha and R. Raj, *J. Am. Ceram. Soc.*, **97**, 527–534 (2014).
8) H. Yoshida, Y. Sakka, T. Yamamoto, J.-M. Lebrun and R. Raj, *J. Eur. Ceram. Soc.*, **34**, 991–1000 (2014).
9) M. Cologna, A. L. G. Prette and R. Raj, *J. Am. Ceram. Soc.*, **94**, 316–319 (2011).
10) M. Cologna, J. S. C. Francis and R. Raj, *J. Eur. Ceram. Soc.*, **31**, 2827–2837 (2011).
11) R. Muccillo and E. N. S. Muccillo, *J. Eur. Ceram. Soc.*, **34**, 915–923 (2014).
12) X. Hao, Y. Liu, Z. Wang, J. Qiao and K. Sun, *J. Power Sources*, **210**, 86–91 (2012).
13) E. Zapata-Solvas, S. Bonilla, P. R. Wilshaw and R. I. Todd, *J. Eur. Ceram. Soc.*, **33**, 2811–2816 (2013).
14) R. I. Todd, E. Zapata-Solvas, R. S. Bonilla, T. Sneddon and P. R. Wilshaw, *J. Eur. Ceram. Soc.*, **35**, 1865–1877 (2015).
15) Y. Dong and I. W. Chen, *J. Am. Ceram. Soc.*, **98**, 2333–2335 (2015).
16) Y. Dong and I. W. Chen, *J. Am. Ceram. Soc.*, in press. [DOI: 10.1111/jace.13866] (2015).
17) H. Qian and J. Luo, *Acta Mater.*, **56**, 4702–4714 (2008).
18) H. J. Qian and J. Luo, *Appl. Phys. Lett.*, **91**, 061909 (2007).
19) M. Samiee and J. Luo, *J. Power Sources*, **245**, 594–598 (2014).
20) R. Raj, *J. Eur. Ceram. Soc.*, **32**, 2293–2301 (2012).
21) D. W. Kim, T. G. Kim and K. S. Hong, *J. Am. Ceram. Soc.*, **81**, 1692–1694 (1998).